

Robust Phase Retrieval with Green Noise Binary Masks

QIULIANG YE,¹ YUK-HEE CHAN,¹ MICHAEL G. SOMEKH,^{2,3} AND DANIEL P.K. LUN^{1,*}

¹*Department of Electronic and Information Engineering, The Hong Kong Polytechnic University, Hung Hom, Kowloon, Hong Kong*

²*Center for Nanophotonics, Shenzhen University, Shenzhen PRC 518060, People's Republic of China*

³*Faculty of Engineering, University of Nottingham, Nottingham NG7 2RD, United Kingdom*

*enpklun@polyu.edu.hk

Abstract: Phase retrieval with pre-defined optical masks can provide extra constraint and thus achieve improved performance. Recent progress in optimization theory demonstrates the superiority of random masks in phase retrieval algorithms. However, traditional approaches only focus on the randomness of the masks but ignore their non-bandlimited nature. When using these masks in the reconstruction process for phase retrieval, the high-frequency part of the masks is often removed in the process and thus leads to degraded performance. Based on the concept of digital halftoning, this paper proposes a green noise binary masking scheme that can significantly reduce the high-frequency content of the masks while fulfilling the randomness requirement. The experimental results show that the proposed green noise binary masking scheme outperforms the traditional ones when using in a coded diffraction pattern phase retrieval system.

© 2021 Optical Society of America under the terms of the [OSA Open Access Publishing Agreement](#)

1. Introduction

Many measurement systems can only detect the intensity of the optical wave field. Phase retrieval, as the name suggests, aims to reconstruct a complex-valued signal from intensity-only measurements [1–4]. The phase retrieval problem is encountered in several disciplines, including crystallography, optical imaging, astronomy, X-ray and electronic imaging. There has been considerable recent progress in phase retrieval algorithms due to the advent of modern optimization theories [5]. In particular, the so-called coded diffraction pattern (CDP) phase retrieval algorithm adopts pre-defined optical masks to improve the reconstruction performance with extra constraints [6, 7]. Specifically, the algorithm reconstructs a signal $\mathbf{U} \in \mathbb{C}^n$ (complex-valued) based on the Fourier intensity measurements $y_i = |\mathcal{F}(\mathbf{I}_i \circ \mathbf{U})|^2$, $i = 1, \dots, M$, where M , \mathbf{I} and \circ denote the number of measurements, pre-defined optical masks and elementwise multiplication, respectively; and \mathcal{F} is the Fourier transform. In practice, the pre-defined masks can be implemented using a spatial light modulator (SLM) or digital micromirror device (DMD) [8–11]. The number of measurements is related to the complexity of the signal and the masks. For instance, the single-shot lensless phase retrieval methods in [9, 10] require only a single measurement, but it can reconstruct only sparse objects. On the other hand, using multiple-level phase masks can also reduce the number of measurements. However, they require optical devices that can perform accurate multi-level phase modulation for their implementation. The cost of these devices is one concern; the error of these devices due to the global grayscale-phase mismatch and spatial non-uniformity is another. If binary masks are used, it is empirically shown in [6, 7] that at most 6 measurements are required for exact recovery via convex programming. Thus, the number of measurements is not excessive. Binary masks can provide accurate reconstruction as the two levels can be reliably reproduced; these can be realized with both DMDs and SLMs. For this reason, binary masks are used in this work.

To ensure good phase retrieval performance, the importance of the randomness of the masks

is emphasized in [6, 7]. Thus, white noise masks are used traditionally since the randomness is guaranteed. However, the Fourier spectrum of white noise masks is non-bandlimited in theory (an example is shown in Fig. 1). We will show later that in practice only the 0th diffraction order of the intensity measurements can be used for the phase retrieval algorithm. It means that some high frequency components of the masks will be filtered out and this introduces error to the optimization process. In this paper, we base on our previous work [12] on digital halftoning to propose a green noise optical masking scheme for phase retrieval. The proposed scheme allows the optical masks to have the green noise property. The Fourier transform of the mask is concentrated in a ring shape mid-frequency region so that the amount of the filtered high-frequency components can be reduced. Halftoning is a process which is commonly used in digital printers to simulate shades of gray by varying the size of tiny black dots. Recently, we apply the multiscale error diffusion (MED) technique to the halftoning process so that we can control the black dot patterns to have the green noise property [12]]. Such technique can also be used in the optical mask generation. One advantage of the scheme is that we can generate the binary masks of different densities (the ratio of the number of ones to zeros in the masks) while maintaining the green noise property. The density of the masks needs to be carefully chosen to avoid the saturation problem when taking the measurements. Using the proposed green noise masking scheme, the error in the reconstructed phase can be reduced compared with the traditional white noise masks. It has been verified with our experimental results in Section 4.

2. Phase Retrieval with Coded Diffraction Patterns

The objective of the CDP phase retrieval algorithm [6, 7] can be described by Eq. (1).

$$\text{Find } \mathbf{U} \in \mathbb{C}^n \quad \text{s.t.} \quad \mathbf{y}_i = |\mathcal{F}(\mathbf{I}_i \circ \mathbf{U})|^2, i = 1, \dots, M, \quad (1)$$

where \mathbf{y}_i is a Fourier intensity measurement and $\mathbf{x} \circ \mathbf{y}$ denotes the elementwise multiplication of \mathbf{x} and \mathbf{y} . The use of the optical masks \mathbf{I} provides the constraints to reduce the ill-posedness of the problem. It has been shown in [6, 7] that \mathbf{U} can be perfectly reconstructed from noiseless measurements \mathbf{y} with high probability given \mathbf{I} are random and M . However, in a coherent imaging system, speckle noise inherent in the laser and shot noise due to the limited photon measurements are prevalent. They bring errors to the Fourier intensity measurements and corrupt the reconstructed phase. The maximum a-posterior (MAP) method is often used to ensure the performance of the estimation. It is applied for estimating the maximum point of an unknown quantity with the help of a posterior distribution. To further improve the optimization performance, different regularization terms are added to the optimization cost function. In this work, we adopt the total variation (TV) regularization term to smooth out the noise while preserving the image edges [13]. Combining with the MAP formulation, we adopt the following TV-MAP approach [13] for the implementation of the CDP phase retrieval algorithm in this paper:

$$\begin{aligned} \min_{\mathbf{U} \in \mathbb{C}^n} \quad & \alpha \|\nabla \hat{\mathbf{U}}\|_1 + \frac{1}{2} \sum_i \left(|\mathbf{g}_i|^2 - \hat{\mathbf{y}}_i \log |\mathbf{g}_i|^2 \right) \\ \text{s.t.} \quad & \mathbf{g}_i = \left| \text{DFT}(\hat{\mathbf{i}}_i \circ \hat{\mathbf{U}}) \right|^2, i = 1, \dots, M \end{aligned} \quad (2)$$

In Eq. (2), ∇ is the gradient operator, $\|\cdot\|_1$ refers to the ℓ_1 norm and DFT refers to the discrete Fourier transform; and $\hat{\mathbf{y}}$ represents the discrete Fourier intensity measurements which are the sampled version of \mathbf{y} . Similarly, $\hat{\mathbf{I}}$ and $\hat{\mathbf{U}}$ are the discrete estimates of \mathbf{I} and \mathbf{U} , respectively. The first term of Eq. (2) is the TV regularization term that has been popularly used in noise removal. It is based on the principle that images with spurious details have higher total variation. Reducing the total variation of the measurement can remove the unwanted details. The second

term of Eq. (2) is the MAP data fidelity term that evaluates the performance of the estimation. Minimizing these two terms can obtain an estimate that is close to the original $\hat{\mathbf{U}}$ while reducing the spurious detail due to noise. Furthermore, the optimal solution allows discontinuities along the curves; therefore, edges can be preserved in the restored image. The regularization strength is controlled by the constant α . It is usually selected empirically according to the complexity of the signal. Similar to [6, 7], Eq. (2) can be solved via the Alternating Direction Method of Multipliers (ADMM) algorithm [14].

For obtaining the measurements \mathbf{y}_i , the light will first go through a lens so that the image captured by the sensor is the Fourier transform of the transmittance function of the object \mathbf{U} multiplied with the i -th mask \mathbf{I}_i . As mentioned in Section 1, binary masks are used in this work. Both SLM and DMD can be used to implement \mathbf{I} . When SLM is used, \mathbf{I} can be implemented as a set of binary phase masks such that $\mathbf{I} \in \{e^{i\theta}, e^{i\pi}\}$. If DMD is used, \mathbf{I} becomes a set of binary amplitude masks such that $\mathbf{I} \in \{0, 1\}$. A typical experimental setup for implementing the CDP phase retrieval system is shown in Fig. 2. In this optical system, the light from the HeNe laser is projected onto a SLM or DMD board which implements the random masks. The masked light is projected onto an object placed on the image plane. The light then goes through a lens and a CMOS camera placed on the back focal plane of the lens collects the intensity images of the periodic Fourier spectrum for further processing. The setup in Fig. 2 is also adopted in our experiments. Mathematically, the optical field in the back focal plane behind the lens can be modeled by the following formulation [15]:

$$\tilde{\mathbf{x}}_i(u, v) = C \sum_k \sum_l \mathbf{x}_i \left(u - \frac{k\lambda f}{d}, v - \frac{l\lambda f}{d} \right) \text{sinc}(\Theta(k, l)) \text{sinc}(\Phi(u, v)), \quad (3)$$

where C , d , f and λ denote the scaling constant, the distance between micro-display units, focal length and wavelength, respectively; and $\mathbf{x}_i = \mathcal{F}(\mathbf{I}_i \circ \mathbf{U})$. Θ and Φ are functions related to the pixelated SLM or the geometrical structure of the micromirrors of DMD [15]. Eq. (3) shows that the optical field is a replica of \mathbf{x}_i attenuated by two *sinc* functions. Overall, the intensity measurements of $\tilde{\mathbf{x}}$ appear as a kind of diffraction pattern as shown in Fig. 1.

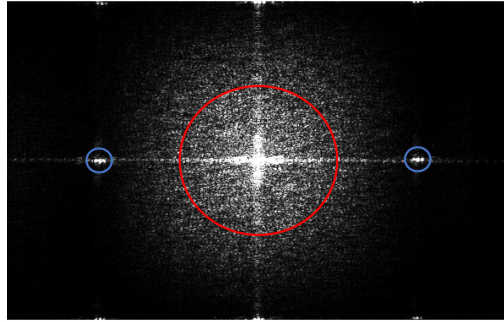


Fig. 1. Fourier intensity measurement (in log scale) of a USAF chart multiplied with a white noise mask. Red circle denotes the 0th diffraction order detected in the optical system with optimized numerical aperture. Blue circles represent the central areas of the 1st diffraction order. The white noise mask introduces many high frequency components that are beyond the red circle.

As mentioned above, the reconstruction algorithm for solving Eq. (2) is a discrete process. In each iteration, the discrete estimation of \mathbf{U} , i.e. $\hat{\mathbf{U}}$, is used to compute $\hat{\mathbf{g}}_i = |DFT(\hat{\mathbf{I}}_i \circ \hat{\mathbf{U}})|^2$ and then evaluated the MAP loss function with the discrete measurement $\hat{\mathbf{y}}$. The sampling period of $\hat{\mathbf{I}}_i$ and $\hat{\mathbf{U}}$ is d , i.e. the distance of the SLM pixels or the micro-display units of the DMD. As

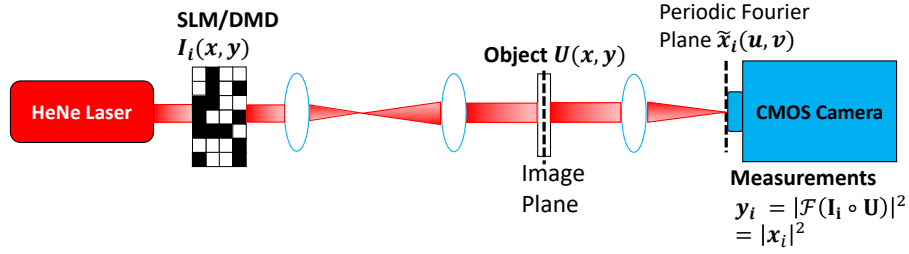


Fig. 2. Experimental setup of the CDP phase retrieval system.

the property of DFT, $\hat{\mathbf{g}}_i$ will cover only one period of the replicated spectrum, i.e. from $-\frac{\lambda f}{2d}$ to $\frac{\lambda f}{2d}$, which coincides with the boundaries of the 0th diffraction order of the Fourier intensity measurement (the red circle in Fig. 1). In fact, only the 0th diffraction order can be detected and the data of higher orders are not available in practical optical system with the maximum numerical aperture. For this reason, any data of $\hat{\mathbf{y}}_i$ outside the 0th diffraction order will not be considered in the optimization process.

Traditionally, the optical masks \mathbf{I} are often implemented by white noise patterns since only the randomness of the masks are considered. However, white noise is non-bandlimited in principle. There is a significant amount of high-frequency components for white noise masks that are outside the 0th diffraction order (as shown in Fig. 1). The discrete optimization process will ignore these coefficients and thus degrade the phase retrieval performance. We will verify such phenomenon experimentally in Section 4.

3. Green Noise Binary Masks

3.1. Generation of the Green Noise Masks

While it is inevitable that the high-frequency data outside the 0th diffraction order will be ignored during the optimization process, we can reduce the distortion by limiting the high-frequency components of the masks. To this end, we use green noise masks which have their energy concentrated in the mid-frequency region. The Fourier intensities (in log scale) of some examples of green noise masks are shown in Fig. 3. As can be seen in the figure, the energy of the masks concentrates in the ring in the middle of the Fourier spectrum. Thus, the high frequency energy of the mask is significantly reduced. The green noise masks in Fig. 3 are designed based on a digital halftoning method called FMEDg that we proposed in [12]. Digital halftoning is a process for turning a grayscale image into a binary image such that it can be physically printed [16]. When the input is a constant grayscale patch, the output of digital halftoning is a binary noise pattern composed of black (0) and white (1) dots. We make use of the digital halftoning method FMEDg in this research because it can generate binary noise patterns that fully fulfill the needs of a CDP phase retrieval process. First, the output of digital halftoning is a set of black and white dots, which is the same as a binary mask. Second, the method can ensure the spatial distribution of the dots to be aperiodic, homogeneous and isotropic. Thus, it can fulfill the randomness requirement. More importantly, we can control the frequency response of the output noise pattern (from green to blue) and its density (i.e. the ratio of the number of ones to zeros in the masks). The algorithm starts with a mask with a constant value, for instance, 0.5. Then an iterative feature preserved multiscale error diffusion (FMED) approach [17] is used to process each pixel in the mask. More specifically, we select a not-yet processed pixel and quantize its value to be either 0 or 1. Then the quantization error is diffused to the pixel's neighbors with a ring-shaped non-causal diffusion filter. This process repeats until all pixels are processed. One can refer to [12] for the operation details. Since the method, which is based on

FMED, can generate green noise patterns, the method is named as FMEDg. In that method, the diffusion filter plays a critical role in controlling the frequency response of the output pattern. Let us illustrate it by an example. Without loss of generality, we assume that pixel $(0, 0)$, which has the initial value of 0.5, is the pixel picked at a particular iteration. Assume it is quantized to 0, FMEDg will diffuse the quantization error, i.e. 0.5, to a ring-shaped region surrounding the pixel as shown in Fig. 4. The process is controlled by the following diffusion filter:

$$D(m, n) = \frac{A(m, n, R_2) - A(m, n, R_1)}{(R_2^2 - R_1^2) \pi}, \quad (4)$$

where $A(m, n, R_k)$ is a function such that,

$$A(m, n, R_k) = \begin{cases} 1, & \sqrt{m^2 + n^2} \leq R_k, \quad k = 1, 2 \text{ and } R_2 > R_1 \\ 0, & \text{otherwise} \end{cases} \quad (5)$$

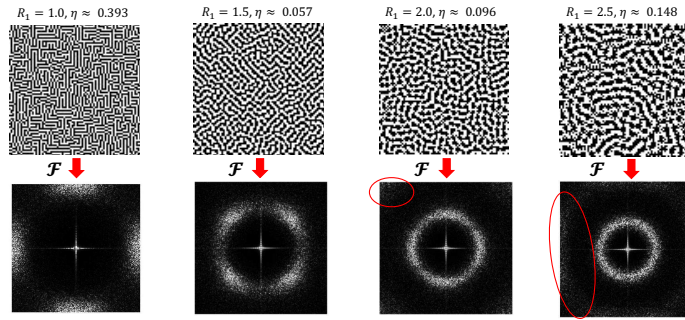


Fig. 3. Spatial domain, Fourier domain (in log scale) and energy concentration ratio of green noise masks of different R_1 with $\sigma = 0.5$. The parameter η is defined as the amount of energy with frequency greater than 0.8 of the maximum range.

More specifically, the error 0.5 will be multiplied by $D(m, n)$ and added to the pixel (m, n) if (m, n) is located inside the ring-shape region determined by the outer radius R_2 and inner radius R_1 . In [12], we show that by setting $R_2 = \sqrt{2}R_1$, we can control the cluster size of the noise pattern to be approximately equal to $R_1^2 \pi \sigma$, where σ is the initial constant gray level of the mask and is also the final density of the noise pattern. The larger is the cluster size of the noise pattern, the lower the frequency response will be. And since the filter is isotropic, the frequency response of the noise pattern will appear as a ring-shaped pattern shown in Fig. 3. Thus, by following the FMEDg method, we can generate a green noise mask of any principal frequency and density σ by simply adjusting the parameter R_1 of the diffusion filter.

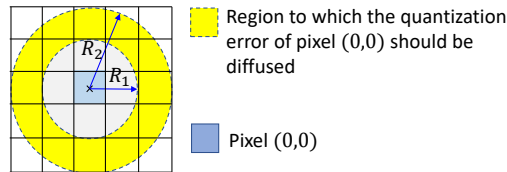


Fig. 4. An illustration of the ring-shape diffusion filter.

3.2. Analysis of the Green Noise Mask Generated by the FMEDg Method

Fig. 3 shows some examples of the green noise masks of different R_1 generated by the FMEDg method (with the density σ fixed at 0.5). Here we would like to introduce another parameter η which indicates the energy of the mask in the high-frequency region of the spectrum. We define η as,

$$\eta(\mathbf{i}) = \frac{\sum_{m,n} \mathbf{i}(m,n > 0.8N)}{\sum_{m,n} \mathbf{i}(m,n)}, \quad (6)$$

where $\mathbf{i} = |DFT(\mathbf{I})|^2$ and N is the total number of DFT coefficients. It can be seen in Fig. 3 that, as R_1 increases, the noise pattern in the mask becomes clustered and the ring shape frequency spectrum shrinks towards the center. Thus, the principal frequency of the noise pattern decreases. However, the high-frequency energy of the masks (indicated by η) does not decrease as the principal frequency decreases. Rather, it first decreases but then increases as R_1 further increases. It is because as the ring shape frequency spectrum shrinks towards the center, another ring starts to appear at the high-frequency spectrum (circled in Fig. 3).

If a mask contains more high-frequency information, the larger the degradation will result as more high-frequency components will be ignored during the phase retrieval process. To demonstrate how the high-frequency information of the mask affects the phase retrieval result, a simple simulation is conducted. We use two standard images namely Cameraman and Barbara (see Fig. 6(a)) as the amplitude and phase part of the input image. Then we multiply the image with the proposed green noise mask (with $R_1 = 1.5$ and $\sigma = 0.5$), blue noise mask and traditional white noise mask [6]. The binary amplitude masks $\mathbf{I} \in \{0, 1\}$ are used in the simulation. Fig. 5 shows the masks and their Fourier intensities. For each kind of mask, 3 Fourier intensity measurements ($M = 3$) are acquired and fed to the same CDP phase retrieval process described in Eq. (2). To show the importance of the high-frequency information, we set the highest 20% frequency data to zero for each Fourier intensity measurement. The performance is evaluated by two criteria: sum square error (SSE) of the amplitude and phase which are defined as follows:

$$\begin{aligned} SSE_{\text{amplitude}} &= 10 \log_{10} \frac{\sum_{i=0}^{N-1} \sum_{j=0}^{M-1} (|u_{i,j}| - |\tilde{u}_{i,j}|)^2}{\sum_{i=0}^{N-1} \sum_{j=0}^{M-1} (|u_{i,j}|)^2}, \\ SSE_{\text{phase}} &= 10 \log_{10} \frac{\sum_{i=0}^{N-1} \sum_{j=0}^{M-1} (|\angle u_{i,j} - \angle \tilde{u}_{i,j} - \phi|)^2}{\sum_{i=0}^{N-1} \sum_{j=0}^{M-1} (|\angle u_{i,j}|)^2}, \end{aligned} \quad (7)$$

where u , \tilde{u} and ϕ denote the original image, reconstructed image, and the global phase shift (a fixed constant), respectively. The values of SSE are usually negative and expressed in dB. The smaller is the value of SSE, the better is the performance.

The reconstruction performance using different masks are shown in Fig. 6(b). It can be seen that the blue noise mask ($\eta = 0.327$) gives the worst result since it has the highest high-frequency concentration. The white noise mask ($\eta = 0.181$) which is commonly used in the literature also does not give a good result, since its high-frequency concentration is still significant. The green noise mask ($\eta = 0.057$) on the other hand gives the best performance both quantitatively and qualitatively. Table 1 shows that the performance differences of the masking schemes are consistent at different noise levels. In real situation, the high-frequency information that will be ignored is at a bit higher frequency than those in this simulation (greater than $\pm\pi$) as explained in Section 2. We cannot simulate such a situation since all digital images do not have frequency information beyond $\pm\pi$. In particular, we do not know their Fourier intensity beyond $\pm\pi$ after multiplying with the masks. However, this simulation has indicated how the high-frequency data affect the phase retrieval process. In Section 4, we shall further demonstrate the real performance of using different noise masks in a CDP phase retrieval system.

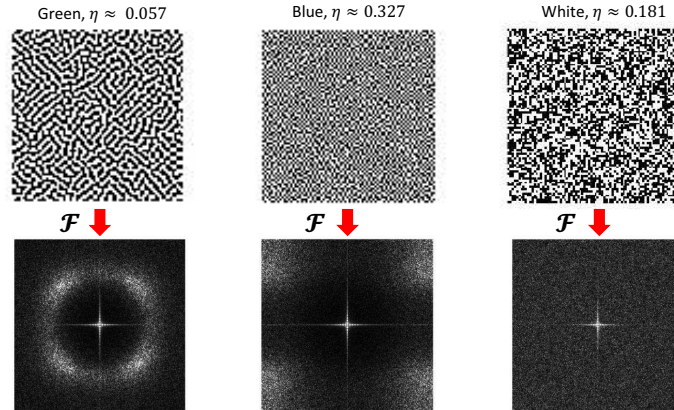


Fig. 5. Spatial domain, Fourier domain (in log scale) and energy concentration ratio of different kinds of binary masks.

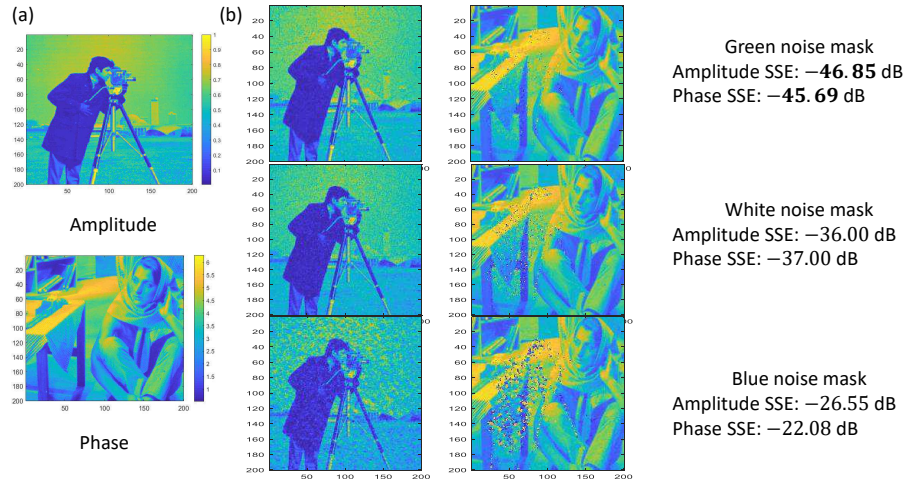


Fig. 6. (a) Simulation images: Cameraman + Barbara. (b) Reconstruction results of using the green, blue and white noise masks when 20% of the highest frequency data are set to 0. The same Poisson and Gaussian noises (SNR ~ 26.5 dB) are added to the Fourier intensity images in each case. In this simulation, 3 Fourier intensity images ($M = 3$) are used for each noise mask.

Table 1. A comparison of the performance when using different noise masks at different noise levels

Mask \ SNR (dB)	Green		White		Blue	
	Amplitude SSE (dB)	Phase SSE (dB)	Amplitude SSE (dB)	Phase SSE (dB)	Amplitude SSE (dB)	Phase SSE (dB)
22.5	-31.13	-22.44	-27.36	-20.19	-12.98	-10.83
24.5	-36.14	-28.71	-29.19	-24.18	-17.88	-15.08
26.5	-42.54	-42.62	-37.44	-33.94	-25.61	-20.96

3.3. The Choice of R_1 and σ

As mentioned above, the parameters R_1 and σ of FMEDg should be carefully chosen. We use the following simulation to show how they will affect the performance of the phase retrieval process. First, we use the FMEDg method to generate a few green noise masks of different R_1 and σ . The binary amplitude masks $\mathbf{I} \in \{0, 1\}$ are used in the simulation. The sizes of the test images and masks are both 200×200 pixels. For each R_1 and σ , 4 green noise masks are generated and multiplied with the images. The DFTs of the resulting images are computed and hence 4 measurements are obtained. Poisson and Gaussian noises are added to the Fourier intensity images in order to simulate the experimental environment. The Fourier intensity images are represented with the 12-bit unsigned integer format to simulate the dynamic range of the camera. We then use the TV-MAP algorithm in Eq. (2) to retrieve the magnitude and phase of the original image. The parameter α of the TV-MAP algorithm is set to 0.1.

The simulation results are shown in Table 2. It can be seen that the SSE decreases as R_1 and σ increase up to a certain limit and then the SSE increases afterward. We have explained in Section 3.2 why the high-frequency information of the mask will increase when R_1 increases beyond a certain limit and degrade the performance. A similar behavior is noted when σ increases. For binary amplitude masks, increasing σ will enlarge the dynamic range of the Fourier intensity image, which will introduce the saturation problem (also exists in the experiment) when σ increases up to a certain value and then affects the performance. In case that the binary phase masks are used, we have also noted in the experiments that saturation problem occurs if σ is set to be bigger than 0.6 or smaller than 0.4. Consequently, the parameters R_1 and σ should be carefully chosen in the experiments. It is indeed an advantage of using the FMEDg method for generating the green noise masks since it allows us to flexibly adjust the parameters R_1 and σ to achieve the required frequency characteristics and density to maximize the performance.

Table 2. Reconstruction performance with respect to different σ and R_1 with green noise masks

$\sigma \backslash R_1$	1.0	1.5	2.0	2.5
0.3	-27.50, -27.18	-33.70, -30.24	-31.01, -29.77	-30.22, -29.67
0.4	-30.20, -27.16	-32.17, -31.45	-33.45, -30.98	-32.51, -30.15
0.5	-31.96, -30.87	-37.88, -35.23	-36.94, -34.50	-36.37, -34.30
0.6	-29.23, -27.59	-33.45, -31.16	-30.61, -31.13	-33.98, -30.85
0.7	-27.23, -20.29	-31.65, -23.80	-29.38, -23.49	-28.49, -22.86

4. Experimental Results

The aim of the experiments is to demonstrate the performance achieved by using the proposed green noise masking scheme in an actual CDP phase retrieval system. It is compared with using the traditional white noise masks [6]. The experimental setup comprises a Thorlabs 10mW HeNe laser with wavelength $\lambda = 632.8$ nm; and a 12-bit 1920×1200 Kiralux CMOS camera with pixel pitch 5.86μ m. For the implementation of the noise masks, a 1920×1080 Holoeye Pluto phase-only SLM with pixel pitch $\delta_{SLM} = 8\mu$ m is used. Only the middle 250×250 SLM pixels are utilized in all experiments. The focal length of the lens behind the SLM is 75 mm. The whole experimental setup is already shown in Section 2 (Fig. 2). Fig. 7 shows a snapshot

of the actual hardware setup.

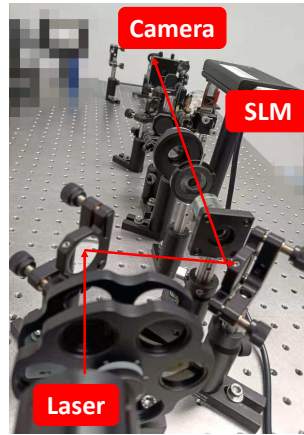


Fig. 7. The actual SLM-based CDP phase retrieval system.

In the experiments, we also use the SLM to generate the testing objects. Specifically, three images namely, Cameraman, Vortex and Cell (see Fig. 8) are loaded to the SLM to generate the phase testing objects that can impose multiple-level phase changes. In this experiment, the binary phase masks $\mathbf{I} \in \{e^{i0}, e^{i\pi}\}$ are used. The images are pre-multiplied with the random masks before sending to the SLM. Thus, the output of the SLM has already implemented the function $\mathbf{I}_i \circ \mathbf{U}$ in Eq. (1). The green noise masks are generated using the FMEDg method described above. Based on the simulation result described in Section 3.3 and further experimental work, we choose $R_1 = 1.5$ and $\sigma = 0.5$ when generating the green noise masks. Only 3 measurements are taken for each kind of binary phase masks. It is worth noting that the fixed constant α in the optimization algorithm controls the strength of regularization. For different experimental objects, the optimal α are different because of their different complexities (curves, sizes, edges, etc.). In our experiments, we fine-tune the values of α to ensure the best SSE is obtained in each case. The experimental results are presented in Fig. 8. It can be clearly seen that the performance of the reconstructed images via the green noise masks are much better than those reconstructed via the white noise masks, both quantitatively and qualitatively. The improvement in SSE can be up to 7.2 dB. The improvement on the cell images is particularly significant.

To demonstrate the generality of the proposed green noise masking scheme, we also apply the scheme to a DMD-based CDP phase retrieval system. A similar experimental setup as in Fig. 2 is used with the SLM replaced by a 1024×768 pixels DMD with pixel pitch $13.68\mu\text{m}$ installed on a Discover 1100 DLP board. Fig. 9 shows a snapshot of the actual hardware setup. In this case, the binary amplitude masks $\mathbf{I} \in \{0, 1\}$ are loaded to the DMD board. In this experiment, a Newport USAF chart is placed on the object plane as the testing object. The projected light can only pass through the chart through its holes thus introduces sharp amplitude changes along the boundaries of the holes. The light that can pass through the chart should have the same phase, and we do not expect there is any variation in phase for the regions with no light. For the experiment, 3 measurements are captured by the camera for each kind of binary masks. They are fed to the same TV-MAP algorithm to retrieve the amplitude and phase of the USAF chart. In this experiment, the empirical optimal α of the TV-MAP algorithm is set as 0.01. Fig. 10 shows the experimental results with different binary masks. It can be seen that the amplitude and phase images retrieved through the use of different kinds of binary masks have clear differences. Even though the background areas of the amplitude images are smooth for all kinds of binary masks, the quality of the images at the regions where light can pass through has considerable

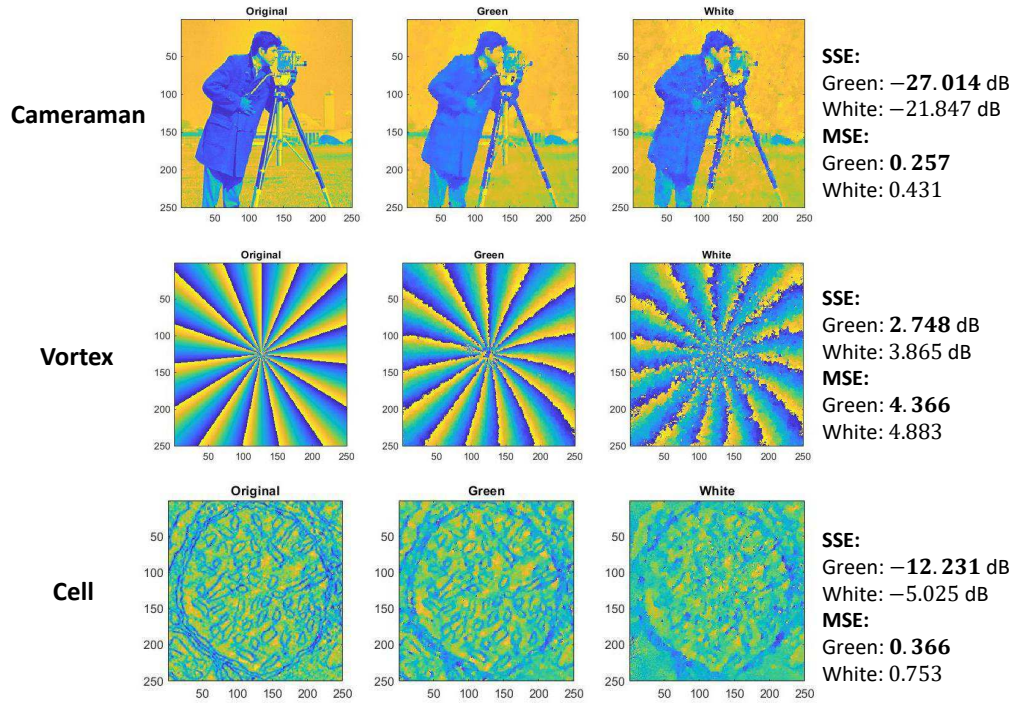


Fig. 8. Experimental results reconstructed via the use of the green and white noise masks.

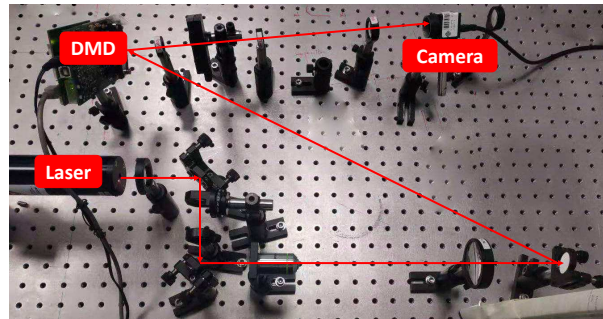


Fig. 9. The actual DMD-based CDP phase retrieval system.

difference. The amplitude image resulting from using the green noise masks remain sharp and relatively uniform. Comparing with those via the white noise masks, we measure the amplitude differences along the red line between the results and ground truth. As can be seen in Fig. 10, the MSE of the amplitude profiles via the green and white noise masks are 0.0222 and 0.0775, respectively. The SSE (dB) are -29.727 and -17.238 , respectively. As for the phase images, the one resulting from using the green noise masks also has a much smoother background and with fewer errors comparing with the white noise masks.

5. Conclusion

This paper proposes a green noise binary masking scheme for the coded diffraction pattern (CDP) phase retrieval systems. We have explained why the high-frequency data in the Fourier

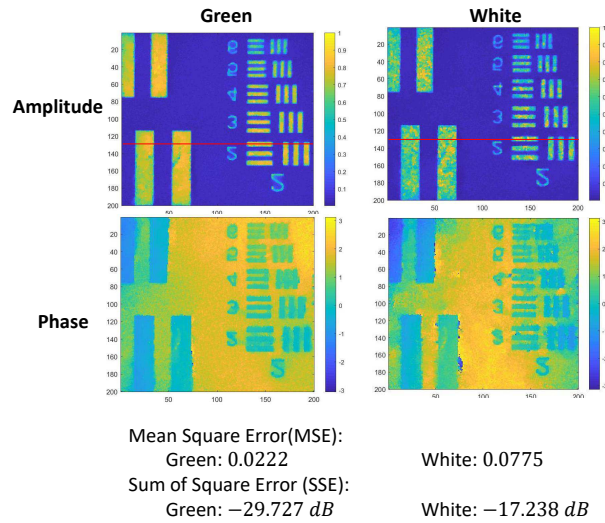


Fig. 10. Experimental results of the USAF chart reconstructed via the use of the green and white noise masks.

intensity measurements will be ignored by the CDP phase retrieval process if they are beyond the 0th diffraction order. To reduce the information loss, we suggested to use the green noise masks which has very low high-frequency concentration. The green noise masks are designed using a digital halftoning method we developed earlier. It has the advantage that the principal frequency and the density of the noise mask can be controlled independently. Also, we have demonstrated how the high-frequency data in the Fourier intensity measurements can affect the quality of the reconstruction images. It is verified by the experimental results, which show that the quality of the amplitude and phase images retrieved using the proposed green noise binary masking scheme outperforms the commonly used white noise binary masks.

References

1. R. W. Gerchberg, "A practical algorithm for the determination of phase from image and diffraction plane pictures," *Optik* **35**, 237–246 (1972).
2. J. R. Fienup, "Phase retrieval algorithms: a comparison," *Appl. Opt.* **21**, 2758–2769 (1982).
3. J. Miao, P. Charalambous, J. Kirz, and D. Sayre, "Extending the methodology of x-ray crystallography to allow imaging of micrometre-sized non-crystalline specimens," *Nature* **400**, 342–344 (1999).
4. J. M. Rodenburg, "Ptychography and related diffractive imaging methods," *Adv. Imaging Electron Phys.* **150**, 87–184 (2008).
5. Y. Shechtman, Y. C. Eldar, O. Cohen, H. Chapman, J. Miao, and M. Segev, "Phase retrieval with application to optical imaging: A contemporary overview," *IEEE Signal Process. Mag.* **32**, 87–109 (2015).
6. E. J. Candes, X. Li, and M. Soltanolkotabi, "Phase retrieval from coded diffraction patterns," *Appl. Comput. Harmon. Analysis* **39**, 277–299 (2015).
7. E. J. Candes, X. Li, and M. Soltanolkotabi, "Phase retrieval via wirtinger flow: Theory and algorithms," *IEEE Transactions on Inf. Theory* **61**, 1985–2007 (2015).
8. C. Falldorf, M. Agour, C. v Kopylow, and R. Bergmann, "Phase retrieval by means of a spatial light modulator in the fourier domain of an imaging system," *Appl. optics* **49** **10**, 1826–30 (2010).
9. R. Horisaki, Y. Ogura, M. Aino, and J. Tanida, "Single-shot phase imaging with a coded aperture," *Opt. letters* **39** **22**, 6466–9 (2014).
10. R. Horisaki, R. Egami, and J. Tanida, "Experimental demonstration of single-shot phase imaging with a coded aperture," *Opt. express* **23** **22**, 28691–7 (2015).
11. C. Zheng, R. Zhou, C. Kuang, G. Zhao, Z. Yaqoob, and P. So, "Digital micromirror device-based common-path quantitative phase imaging," *Opt. Lett.* **42** **7**, 1448–1451 (2017).
12. Y.-H. Fung and Y.-H. Chan, "Green noise digital halftoning with multiscale error diffusion," *IEEE Transactions on Image Process.* **19**, 1808–1823 (2010).

13. H. Chang, Y. Lou, Y. Duan, and S. Marchesini, "Total variation-based phase retrieval for poisson noise removal," *SIAM J. on Imaging Sci.* **11**, 24–55 (2018).
14. S. P. Boyd, N. Parikh, E. Chu, B. Peleato, and J. Eckstein, "Distributed optimization and statistical learning via the alternating direction method of multipliers," *Found. Trends Mach. Learn.* **3**, 1–122 (2011).
15. X. Ding, Y. Ren, L. Gong, Z.-X. Fang, and R. de Lu, "Microscopic lithography with pixelate diffraction of a digital micro-mirror device for micro-lens fabrication," *Appl. Opt.* **53** **24**, 5307–11 (2014).
16. R. Ulichney, *Digital halftoning* (MIT press, 1987).
17. Y.-H. Chan and S.-M. Cheung, "Feature-preserving multiscale error diffusion for digital halftoning," *J. Electron. Imaging* **13**, 639–645 (2004).